Effects of the microstructure and porosity on properties of Ti-6Al-4V alloy fabricated by Electron Beam Melting (EBM)

Authors: Haize Galarraga*1, Diana A. Lados1, Ryan R. Dehoff^{2,3}, Michael M. Kirka^{2,3}

Abstract

Electron Beam Melting (EBM) is a metal powder bed-based Additive Manufacturing (AM) technology that makes possible the fabrication of three dimensional near-net-shaped parts directly from computer models. EBM technology has been in continuously updating, obtaining optimized properties of the processed alloys. Ti-6Al-4V titanium alloy is the most widely used and studied alloy for this technology and is the focus of this work. Several research works have been completed to study the mechanisms of microstructure formation as well as its influence on mechanical properties. However, the relationship is not completely understood, and more systematic research work is necessary in order to attain a better understanding of these features. In this work, samples fabricated at different locations, orientations, and distances from the build platform have been characterized, studying the relationship of these variables with the resulting material intrinsic characteristics and properties (surface topography, microstructure, porosity, micro-hardness and static mechanical properties). This study has revealed that porosity is the main factor controlling mechanical properties relative to the other studied variables. Therefore, in future process developments, decreasing of the porosity should be considered as the primary goal in order to improve mechanical properties.

KEYWORDS: additive manufacturing; electron beam melting; titanium; porosity; properties.

1 Introduction

EBM¹ is a metal powder bed-based AM² technology. AM refers to an advanced technology used for the fabrication of three-dimensional near-net-shaped functional components directly from computer models [1]. ASTM F2792 defines AM as "a process of joining materials to make objects from 3D model data, usually layer upon layer, as opposed to subtractive manufacturing methodologies" [2]. The application of AM technologies in general and of EBM in particular is experiencing a considerable increase in variety and quantity of applications. As the technologies are improving their capabilities, more broadly varying industries are studying and implementing the use of these technologies in order to manufacture an increasing variety of products. Biomedical implant application and aerospace structural parts are the most promising areas for EBM technology. However, the development of EBM technology in these areas is slowed down by lack of standardization which is critical in these industry sectors [3–7].

¹ Worcester Polytechnic Institute, Integrative Materials Design Center, 100 Institute Road, Worcester, MA 01609, USA

² Materials Science and Technology Division, Oak Ridge National Laboratory, Oak Ridge, TN 37831, USA

³ Manufacturing Demonstration Facility, Oak Ridge National Laboratory, Oak Ridge, TN 37831, USA

^{*}Corresponding Author: E-mail address: hgalarraga@wpi.edu

¹ Electron beam melting

² Additive manufacturing

EBM's working principle consists of consecutive cycles where complex geometry parts are fabricated layer by layer. Each solid material level is formed after a metallic powder layer is dispensed and selectively melted. The energy source for the melting or scanning process is a filament which emits an electron beam. This beam is controlled by two magnetic coils, which focus and control the beam's position. The manufacturing parameters are generated and controlled by a software in order to fabricate sound parts with improved mechanical properties, low porosity and surface roughness, and optimized geometrical reproducibility. This software creates scanning algorithms based on the geometry of the part to be manufactured. The main parameters controlled by the software are: minimum and maximum beam current, number of times the beam scan is to be repeated, scanning speed of the electron beam, distance between individual scan lines (line offset), line order for the hatch pattern and rotation angle between consecutive hatches [8].

Microstructure evolution and mechanical properties have been studied for Ti-6Al-4V alloy due to its versatility resulting from the good balance between mechanical properties, castability, plastic workability, heat treatability, and weldability [9]. Ti-6Al-4V has been extensively applied in industry and studied in the laboratory, consequently there is an extensive knowledge base relative to other metal alloys. Mechanical property characterization for EBM Ti-6Al-4V varies widely between sources. Facchini et al. [10] noticed that the ultimate tensile strength (UTS) of EBM built specimens is higher than the wrought or annealed ones, with a lower ductility. However, Koike et al. [11] saw that the UTS and ductility of the cast and wrought Ti-6Al-4V specimens were higher than those of EBM counterparts. The reason for the considerable difference between apparently similar studies can be attributed to the variation in the built parameters, which results in different material features such as composition, microstructure, pore size, and porosity distribution, etc. [12]. Other parameters, such as the specimen orientation or its location on the build platform can also have influence due to anisotropic microstructure of EBM fabricated parts. Static mechanical properties found in the literature for different fabrication conditions are not consistent, deviations are large, and the interpretations of the influence of different fabrication conditions and parameters on the results are contradictory in some of the cases. In order to have a better understanding of these data, statistical analysis has been carried out with tensile test data sampled from the available literature (Table 1) and grouped to compare the average values for different fabrication conditions.

Table 1. Tensile results for different fabrication conditions with average values and relative standard deviations. UTS-refers to ultimate strength, YS-to yield strength, and el-to elongation after fracture [10,13–20]

Alloy	Condition	Orientation	UTS [MPa]	RSD [*] [%]	YS [MPa]	RSD [%]	el [%]	RSD [%]
Ti-6Al-4V	as-fabricated	any	984	9.0	917	9.9	11	35.8
Ti-6Al-4V (ELI**)	as-fabricated	any	911	1.1	810	1.3	13	6.4
Ti-6Al-4V	HIP	any	932	3.8	843	3.5	13	3.0
Ti-6Al-4V	as-fabricated	horizontal	979	8.0	905	8.1	10	32.7
Ti-6Al-4V	as-fabricated	vertical	971	8.2	910	8.6	10	34.9

^{*} Relative Standard Deviation (RSD), the ratio of the standard deviation to the mean

This statistical analysis, shows the difference in properties that can be obtained because the employment of Ti-6Al-4V (ELI) alloy or the effect of HIP (hot isostatic pressing) treatment, with respect

^{**} Extra Low Interstitials

to the conventional composition and "as-fabricated" condition. The influence of the orientation of the sample in relation of the build direction also can be noticed on these data. The highest ultimate tensile strength and yield strength are obtained for the as-fabricated condition, where vertical and horizontal orientation of the samples are included. Data indicate that neither HIP treatment nor ELI composition improves the strength considerably, however, ductility increases in both cases.

The location and orientation of specimens relative to the powder bed and build direction has been studied by a number of researchers for its effect on the temperature profile during fabrication. The difference in the temperature profiles along the build direction (Z axis) is due to the build platform's temperature (650-700°C) and thermal conductivities and heat capacities of the platform and powder materials.-It is thought that the high temperatures of the fabrication chamber leads to α' martensitic phase formed during the fast solidification of the melt pool to transform to the final microstructure consisting of α and β phases. Hrabe et al. [16] have considered that the distance between the manufactured part and the build platform does not significantly affect the microstructure and mechanical properties in general, although ductility was found to decrease with distance to the build platform (from 0 to 25 mm). Hrabe et al. [15] also studied the influence of the location of the part in the build platform plane (X,Y axes). They hypothesized that there would be lower temperatures and greater cooling rates at the outer edges of the build chamber due to the increased deflection of the electron beam. This study revealed slightly higher values for both UTS and YS in the interior of the build platform. The effect of part orientation has also been considered in previous works, contrasting horizontal direction (parallel to build platform) and vertical direction (parallel to build direction) for its effect on mechanical properties. According to Hrabe et al. [15], vertically oriented parts have 30% lower elongation compared to horizontally oriented parts. Orientation in X-Y plane was not found to influence mechanical properties. Rawat et al. [21] reported the fabrication of EBM Ti-6Al-4V waveguide brackets for a spacecraft structure and tensile specimens in varied build orientation. The results show a slightly higher tensile strength in the vertical (Z) orientation than in the horizontal (XY) orientation specimens.

2 Material and methods

2.1 Materials selection and processing conditions

The material base for this study is a sample batch manufactured by ORNL (Oak Ridge National Laboratory). Samples were manufactured from Ti-6Al-4V ELI gas atomized powder provided by Arcam. Ti-6Al-4V ELI contains reduced levels of oxygen, nitrogen, carbon, and iron (Table 2). The powders used in this study are depicted in Figure 1 with a diameter between 45 and 100 µm. The powder has a content of 50% reused and 50% new powders. Reused powder refers to powders employed in previous builds. Once a build is finished, the non-sintered powder is kept in the machine at vacuum atmosphere, so the powder can be reused for the next build. When the powder is reused, its oxygen content can increase affecting the properties of the resultant microstructure[22]. For EBM Ti-6Al-4V, Nandwana et al. [23] indicated that after five builds without added new powder, the oxygen content increased from 0.141 to 0.168 wt%, maintaining the level within specifications. The manufacturing parameters (spot size, scan velocity, sintering route, etc.) were defined by an internal algorithm of the Arcam A2 machine (version 3.2 parameter control software). The build was started after attaining a preheat temperature of 650°C. Each scanning layer was 0.05 mm thick and the average scanning time per layer was one minute

for this batch. No post-treatment was applied to the specimens, except for those where the effect of annealing on the microstructure was studied (section 3.5). Annealing was done using a Thermo Scientific Lindberg/Blue (1.8 kW) furnace and three annealing temperatures (600°C, 700°C and 800°C), for time periods between 10 and 120 hours; samples were air cooled at the end of the process.

Table 2. Standard chemical composition [24] and actual chemical composition of the powder provided by Arcam [25]

	Al	V	С	Fe	0	N	Н	Ti
Ti-6Al-4V ELI (Standard)	5.5-6.5%	3.5- 4.5%	<0.08%	<0.25%	<0.13%	<0.05%	<0.012%	Balance
Ti-6Al-4V ELI (Arcam)	6.0%	4.0%	0.03%	0.1%	0.1%	0.01%	<0.003%	Balance

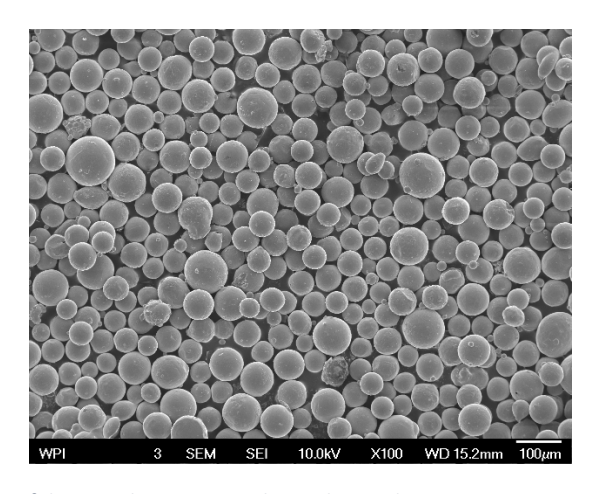


Figure 1. Ti-6Al-4V powders used to fabricate the EBM samples in this study.

2.2 Sample location and preparation

The position and orientation of the samples on the build platform of the Arcam machine are shown in Figure 2. Cylindrical specimens have their longitudinal axis perpendicular to the build platform (parallel to the build direction/Z axis), and rectangular specimens have their longitudinal axis perpendicular to the build direction/Z axis. In this study, the terms *vertical* and *horizontal* orientations are used to identify samples parallel and perpendicular to the build direction/Z axis.

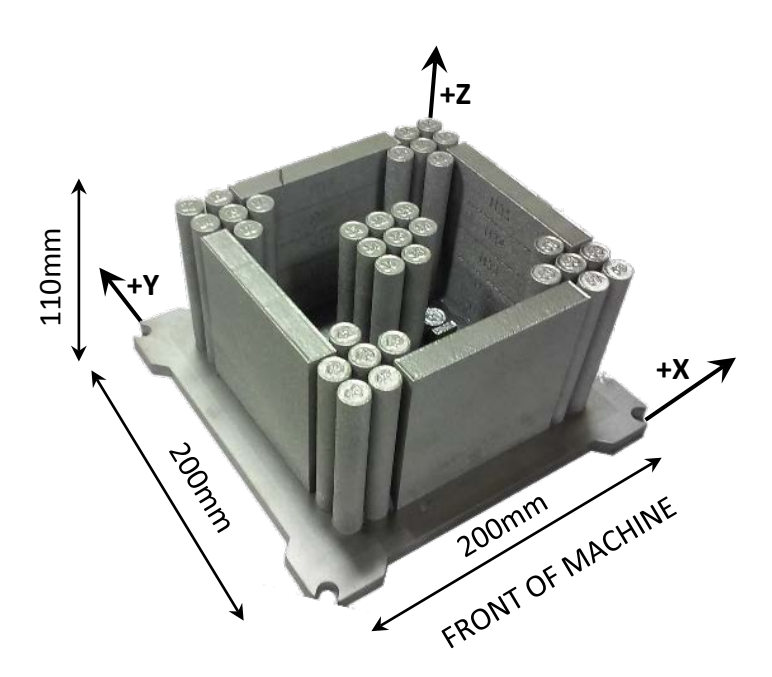


Figure 2. Layout of the specimens on the build platform with the standard Additive Manufacturing axis system [26].

Vertical tensile specimens were machined from the vertical cylinders (D15mm x 105mm), and horizontal tensile specimens were obtained from the large rectangular blocks (15mm x 20mm x 105mm). Vertical cylinders were also used for metallography analysis and porosity quantification at different locations and heights. The microstructural characterization was performed using a small cubic sample (15mm x 15mm x 15 mm) fabricated directly on the build platform. Samples (5mm x 10mm x 10mm) for the annealing studies were obtained from a block located at 90 mm from the build platform in Z axis direction.

2.3 Characterization methodology

2.3.1 Surface topography

Surface topography and roughness were investigated using an Olympus LEXT OLS4100 3D measuring laser microscopy. Surface topography scans were made on a vertical flat plane by Laser Scanning Confocal Microscopy. Confocal microscopy offers several advantages over conventional wide field optical microscopy, including the ability to control depth of field, elimination or reduction of background information away from the focal plane (that leads to image degradation), and the capability to collect serial optical sections from thick specimens [27].

2.3.2 Microstructure and porosity characterization

All samples were cut with an abrasive wheel, mechanically ground, polished with colloidal suspension, and etched with Kroll's reagent. Microstructures were characterized using standard metallographic methods with Nikon's MA 200 Eclipse microscope and image analysis using Elements-D software.

The α lath thickness or interlamellar spacing, representative of typical $\alpha+\beta$ titanium alloy microstructures, was measured employing the method recommended by Vander Voort et al. [28]. The procedure consists of calculating the mean random spacing, σ_r , using the intersection method. The mean random spacing is determined by placing a test grid consisting of one circle of known radius, R, on

the lamellae in an unbiased manner. The number of intersection of the α lamellae with the test line, M, is counted (Figure 3) and divided by the actual length of the test line, to obtain $N_L = 2\pi R/M$. The reciprocal of N_L is the mean random spacing: $\sigma_r = 1/N_L$. The mean true spacing, σ_t , is calculated dividing the mean random spacing by two: $\sigma_t = \sigma_r/2$. This methodology has been applied for five images in each location. These values were averaged to determine the interlamellar spacing at each location.

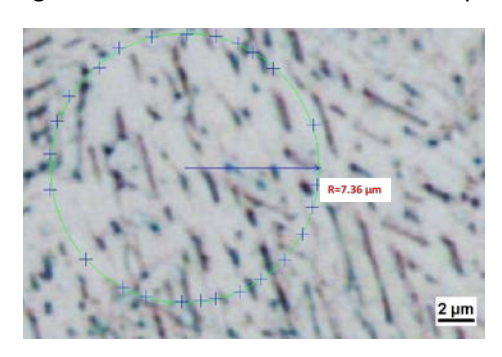


Figure 3. Intersection of α laths on a 7.36 μ m radius circle measured with the image analysis software. The image was obtained in the optical microscope at 1000x magnification and digitally zoomed.

The measurement of the porosity has been performed by image analysis using Elements-D software over micrographs taken at four locations in the vertical direction for each sample (50x magnification). Following the recommendation of Spierings et al. [29], non-etched vertical cross-sections were used for the porosity measurement image analysis.

2.3.3 Micro-hardness

Micro-hardness measurements were made using a TUKON 1202 (Wilson Hardness) machine, with load of 10N applied for 10 seconds. Vertical and horizontal micro-hardness measurements were performed on the build's complete cross-section ($105 \times 15 \text{mm}^2$), in order to determine the influence of distance from the build platform and sample thickness on micro-hardness. Five measurements were taken every 5 mm in the vertical direction and 15 measurements every 2.5 mm in the horizontal direction.

2.3.4 Tensile testing

Tensile specimens were all machined in house using HAAS CNC mill and lathe, with a final dimension of 6 mm diameter and 24 mm gauge length. The geometry and dimensions of the tensile specimens as well as the room temperature tensile tests were performed following ASTM-E8/E8M [30] specifications, using an Instron 5500R frame.

3 Results and discussion

3.1 Surface topography

The surface topography scanning, taken in a vertical oriented plane, revealed an irregular surface (Figure 4a) composed of peaks and valleys. The sintering or scanning layers previously visible at the macroscopic scale cannot be easily distinguished in the scans due to the limited dimension of the measured area $(1.8 \times 2.9 \text{mm}^2)$. However, some elongated valleys parallel to the scanning layers can be observed in Figure 4b, suggesting the existence of a layered pattern on the surface. Safdar et al. [31] described and studied the morphology of this surface and the relation with the fabrication parameters.

Observing the axonometric projection (Figure 4a), it can be noticed that the surface is formed by partially sintered particles. This is confirmed by comparing with the elevation plot of the surface (Figure 4b), where a surface formed by nearly round features can be distinguished. The size of these partially sintered particles (~80µm average) is comparable to the powder particles used for the fabrication of the part (Figure 4c). It is expected that the use of finer powders would result in improved surface finish [32].

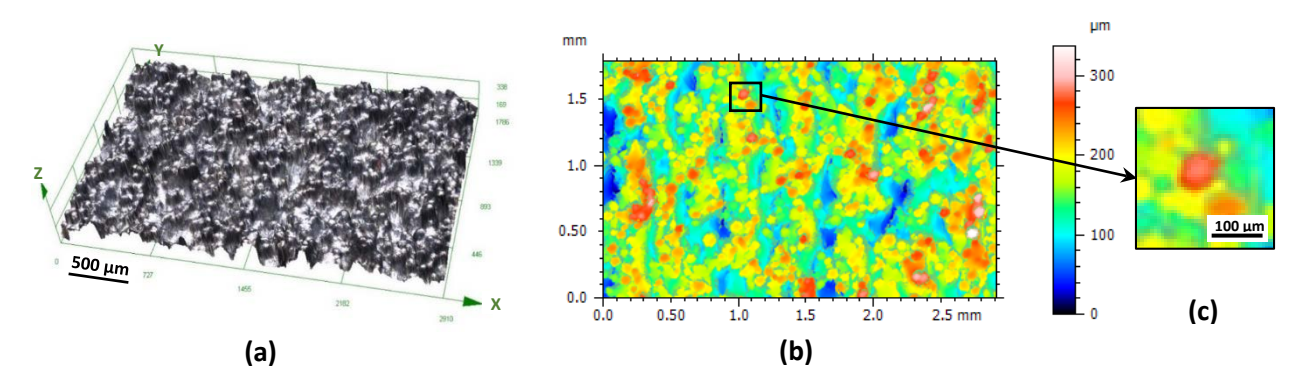


Figure 4. (a) 3D surface scanning of an EBM part; X axis marks the build direction and dimensions are in μ m (b) Scanned surface showing elevation, (c) detailed view with a partially sintered particle in red.

The measurement of the scanned area reveals the following roughness parameters:

Sa (surface average roughness): 45.7 μm

Sp (maximum peak height): 174 μm

Sv (maximum valley depth): 163 μm

The measured area or surface roughness in 3D (Sa=45.7 μ m) is considerably smaller compared to the linear roughness in 2D (Ra=131 μ m) reported by other authors for EBM Ti-6Al-4V in similar conditions [33]. This may be caused because "Sa" covers a surface while the "Ra" is measured along a line that can be influenced by the orientation of the measurement. In the case of additive manufactured parts, the waves formed on the surface by the effect of the scanning layers increase the Ra values on Z direction compared to X and Y directions. In addition, the roughness value is higher than that reported for Selective Laser Melting (SLM), Ra=35 μ m [34], or casting, Ra=10.16 μ m [33]. Roughness of the surface is considered detrimental for the fatigue life of the component because it can serve as stress concentration and fatigue crack initiation site. Nevertheless, the rough surface also can be beneficial for biomedical applications, for example, facilitating the bone structure formation around this surface [35].

3.2 Microstructure characterization

The microstructural characterization was performed using two approaches: the first study was made for different cutting planes through a cubic sample (section 3.2.1), and the second study analyzed the effect of distance from the build plane on microstructure formation (section 3.2.2).

3.2.1 Cutting planes and characteristic phases

In this approach, a cubic sample (15mm x 15mm x 15mm) fabricated on the build platform was analyzed. The sample was prepared by sectioning planes perpendicular to each axis (XY, ZY and XY) to study the microstructure (Figure 5a). A 3D metallographic image was created as shown on Figure 5b.

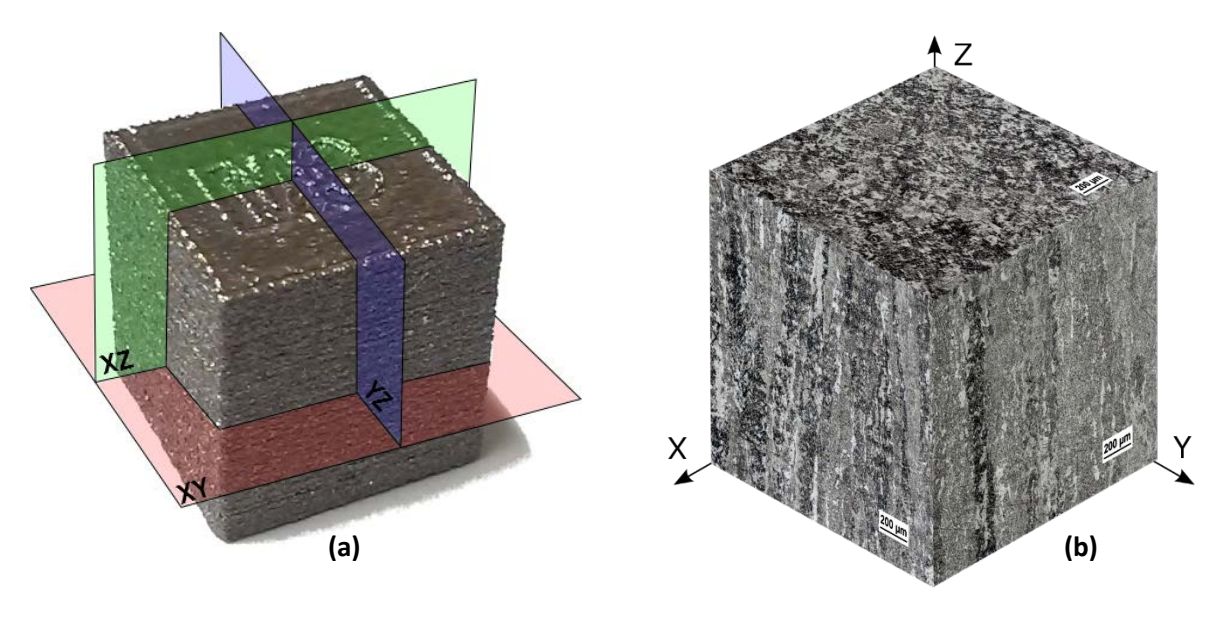


Figure 5. (a) Sectioning planes in the cubic sample, (b) 3D microstructural cube (Z axis represents the build direction).

A prior β columnar structure can be observed in XZ and YZ planes. These columnar structures are oriented parallel to build direction (Z axis). The XY plane shows the microstructure parallel to the scanning layers, where perpendicular sections of the columnar grains can be observed (equiaxed microstructure).

At higher magnification, $\alpha+\beta$ lamellar microstructure is observed inside the prior β grains (Figure 6) for planes both perpendicular and parallel to the build direction. The structure of the lamellae is mainly Widmanstätten or "basket wave", with an occasional colony pattern. The size of the columnar grains is not quantifiable due to the difficulty of the grain boundary identification. However, some of the prior β grain boundaries are delimitated by average 2 μ m thickness α layer (Figure 6b and 6c). This microstructure has been extensively described and characterized in previous studies [13,31,36–38]. At lower magnification, scanning layers are also visible (Figure 7). These layers have an average thickness of 50 μ m, in agreement with the manufacturing parameters.

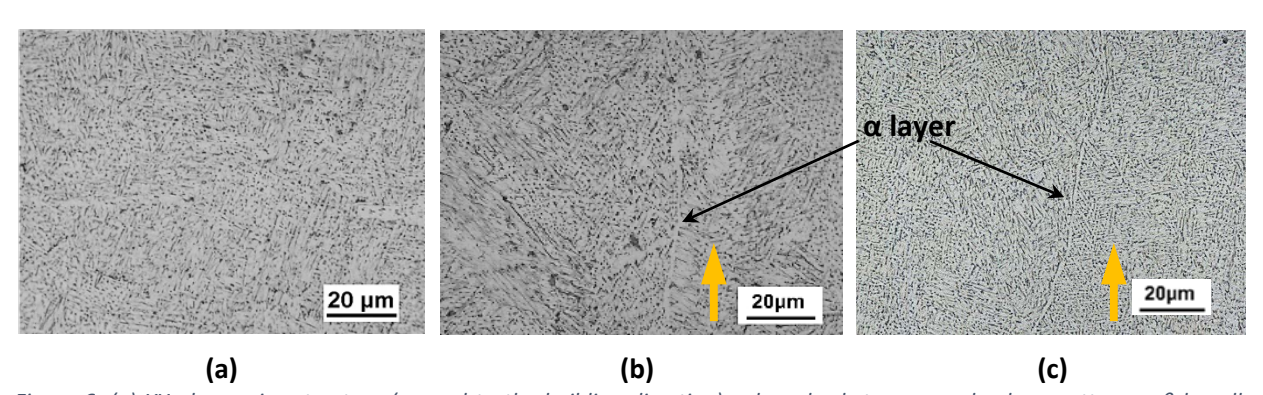


Figure 6. (a) XY plane microstructure (normal to the building direction), where basket wave and colony pattern $\alpha+\beta$ lamellar structure can be observed in equiaxed arrangement. The light phase corresponds to α phase and the dark one to the β phase. (b) and (c) XZ and YZ plane microstructures respectively (parallel to the build direction). Basket wave and colony pattern $\alpha+\beta$ lamellar structure can be observed in columnar arrangement divided by α phase layer at the prior β grain boundaries. The yellow arrows indicate the build direction.

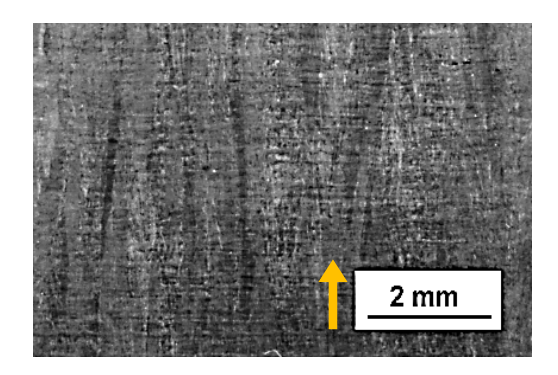


Figure 7. Microstructure and scanning layers in the XZ plane. The build direction is indicated by the arrow.

3.2.2 Effect of location and distance from the build platform on the microstructure

The microstructure was characterized at four more locations to determine the effect of position in the build (Figure 9a). Two specimens were studied in the center of the platform: one at 5mm distance from the platform (CB) and another at 120mm distance (CT). The other two specimens were taken from the front edge of the platform, also at 5mm (EB) and 120mm (ET) heights (Figure 8).

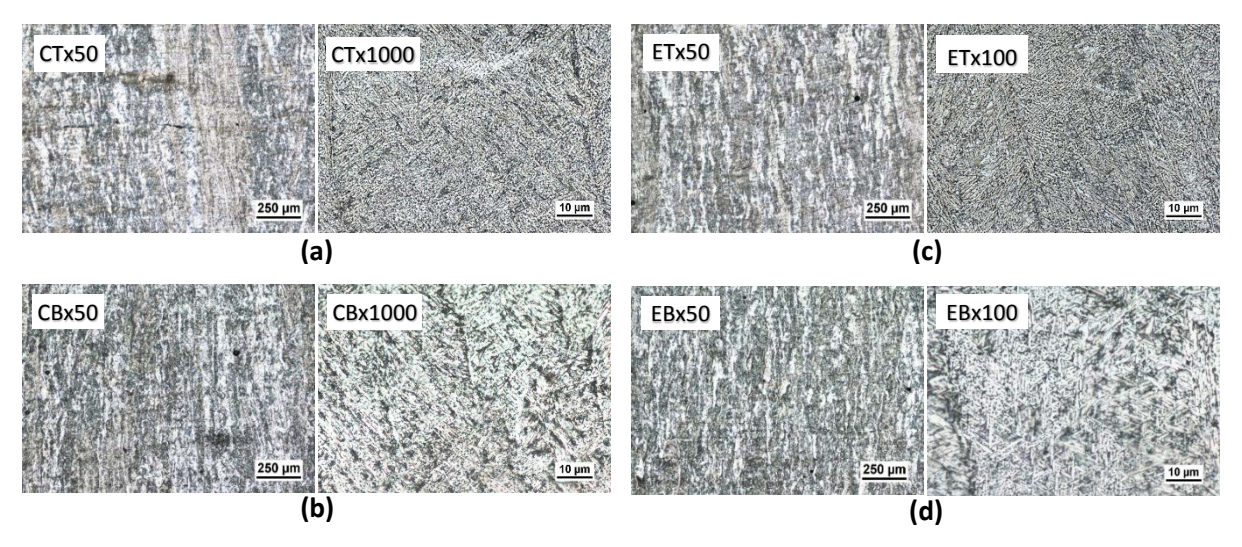


Figure 8. 50x and 1000x micrographs at different positions in the build: (a) center top, (b) center bottom, (c) edge top, (d) edge bottom.

No significant differences were observed between the microstructures of the samples located at the center and at the edge of the build platform. However, at different heights a slight variation in both the β grain size and α lath thickness were identified. The irregular shape of the prior β grains makes accurate quantitative measurement of the thickness difficult, but it is possible to determine that the microstructure look thinner at further to the build platform (specimens CB and EB). Measurements (Figure 9b) indicate that α lath thickness decreases as the distance from the build platform increases, 47% on the center and 34% on the edge. The α lath thickness also varies with respect to the position on the build platform and is 30% lower at the center of the platform. Therefore, the lowest α lath thickness (0.32 μ m) corresponds to the specimen located in the center of the build platform and at 120mm height (CT location). The highest thickness (0.78 μ m) corresponds to the specimen located at the edge of the build platform at 5mm height (EB location).

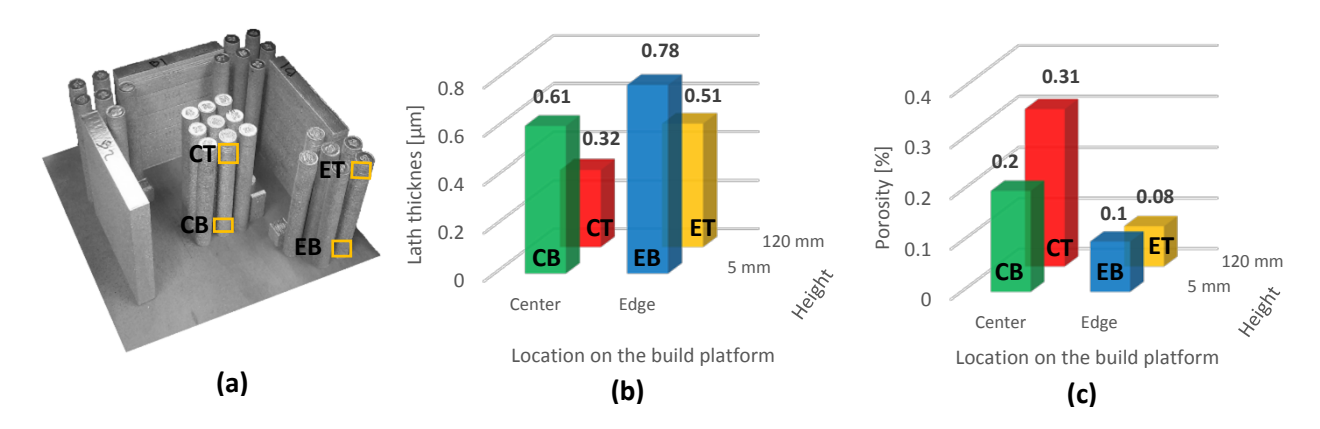


Figure 9. (a) Positions of the studied areas, (b) α lath thicknesses for different locations and heights, (c) porosity values for different locations and heights.

3.2.3 Porosity measurements

From a morphological aspect, detected porosity has been classified in two types: spherical pores (Figure 10a) and irregularly shaped areas parallel to the scanning layers (Figure 10b). The spherical or round shaped voids are originated form the entrapped gas within the gas atomized powder particles [39]. The irregular pores observed represent unmelted areas. This is confirmed by the presence of unmelted powder particles within the irregular pores (Figure 10b). Non-sintered or unmelted zones are attributed to insufficient energy density during the scanning of that area, even though they are not directly correlated [40]. The insufficient energy density may be caused by inappropriate scanning parameters (beam current, scanning velocity, line offset, focus offset, etc.) or other external factors, such as an electromagnetic interference during the fabrication process.

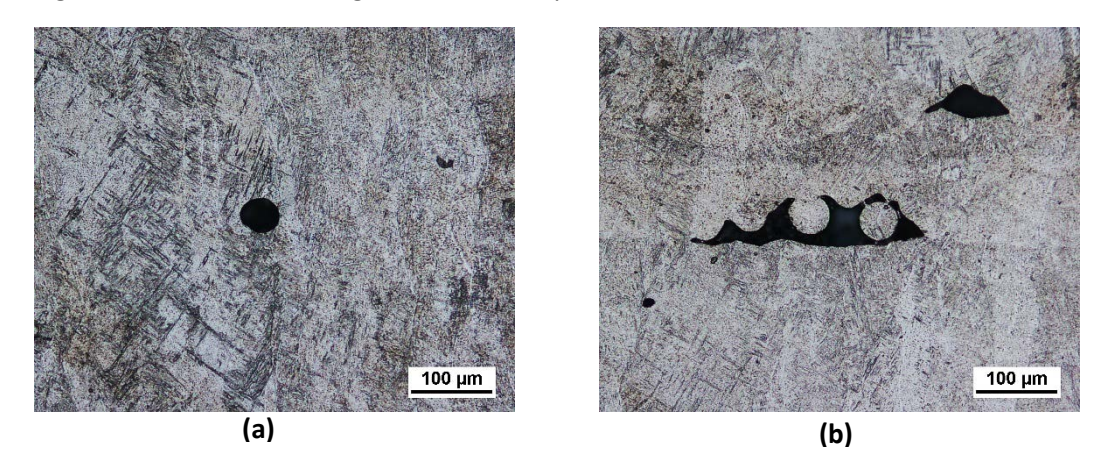


Figure 10. (a) Gas pore (spherical morphology) and (b) non-sintered area or delamination (parallel to the scanning layers) with unmelted particle inside.

In order to study the influence of these defects on mechanical properties, the porosities of the samples at different positions in the build (Figure 9a) were measured. The results indicate that porosity is greater in the center of the build platform (Figure 9c). The obtained average values are 0.09% porosity for samples located at the edge of the build platform and 0.25% for samples located in the center zone. The measured porosity values are consistent with measurements from previous studies [37].

3.3 Micro-hardness measurements

Micro-hardness measurements do not reveal any pattern or variation with the height or width of the EBM parts (

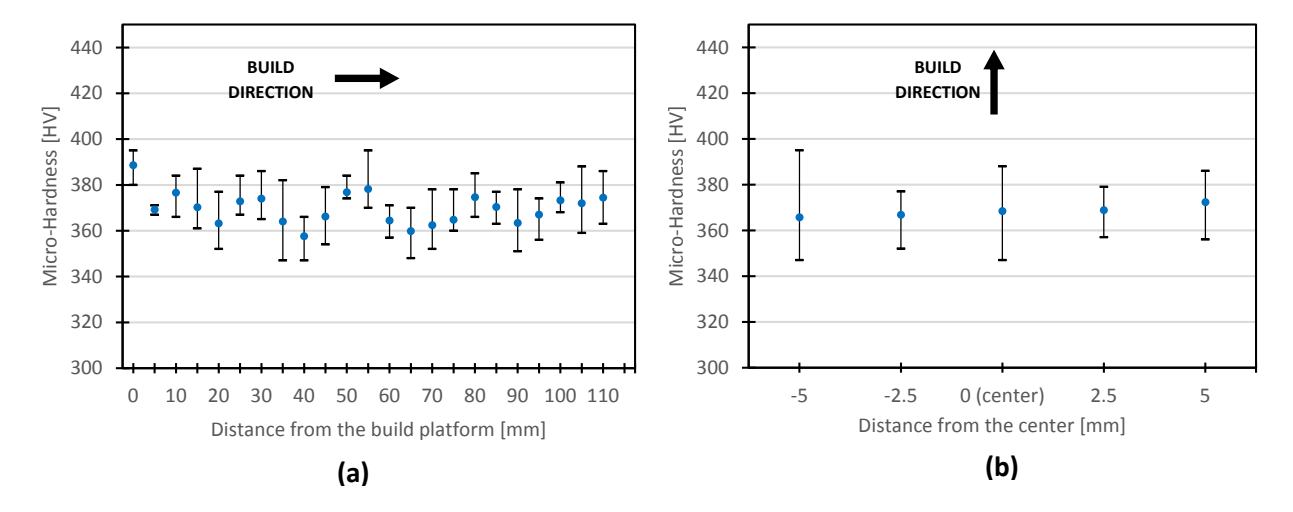


Figure 11). The average value for both orientations (vertical and horizontal) measurements is similar: 368 HV. This value is similar to the values reported in the literature [11,32,41].

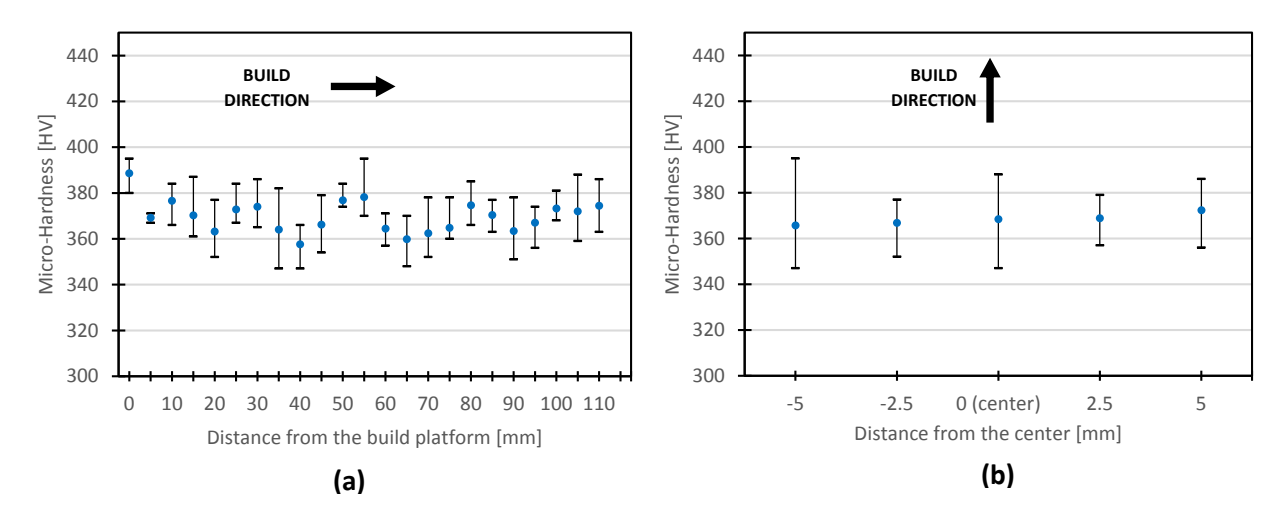


Figure 11. Micro-hardness values for (a) vertical and (b) horizontal directions.

3.4 Tensile properties

Tensile properties were studied with respect to three fabrication variables: distance from the build platform, location on the build platform, and orientation of the samples.

3.4.1 Effect of distance from the build platform on strength and ductility

Tensile tests have been performed on five horizontal oriented specimens at different heights from the build platform, Figure 12, and no significant differences or trends were observed. Yield strength and elongation have greater deviations than the ultimate tensile strength, but no trends relative to the distance from the build platform were found.

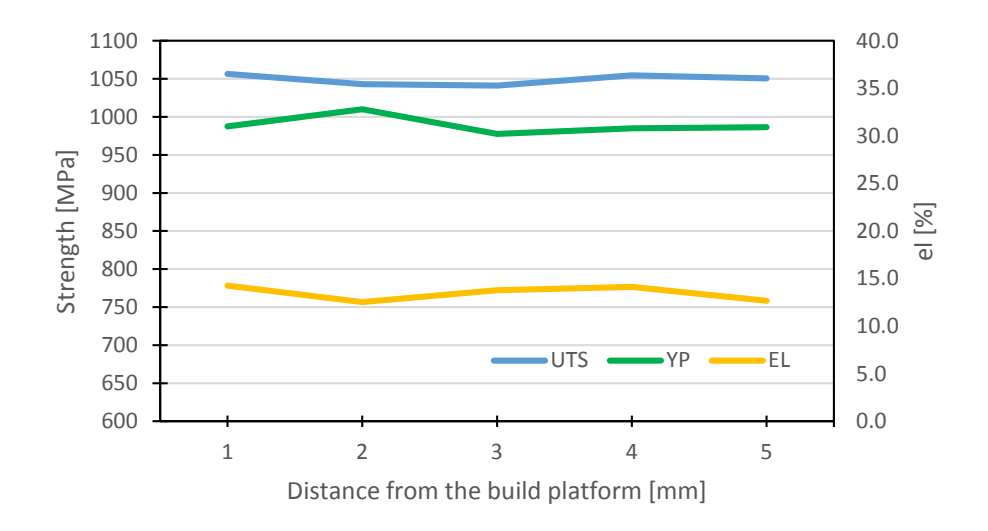


Figure 12. Tensile results for horizontal specimens at different distances from the build platform.

3.4.2 Effect of location on the build platform on strength and ductility

Tensile tests were also performed on vertically oriented specimens at different locations on the platform to assess any effects due to location on the build platform (XY plane). The three locations are the center and the front and rear corners of the build platform, taken on a diagonal. The schematic layout of the specimens and the tensile test results for the three locations are given in Figure 13 and summarized in Table 3. It can be seen that the specimens close to the machine front have higher average values for all three tensile properties (UTS, YS and elongation). Samples taken from the center of the build platform have the lowest values.

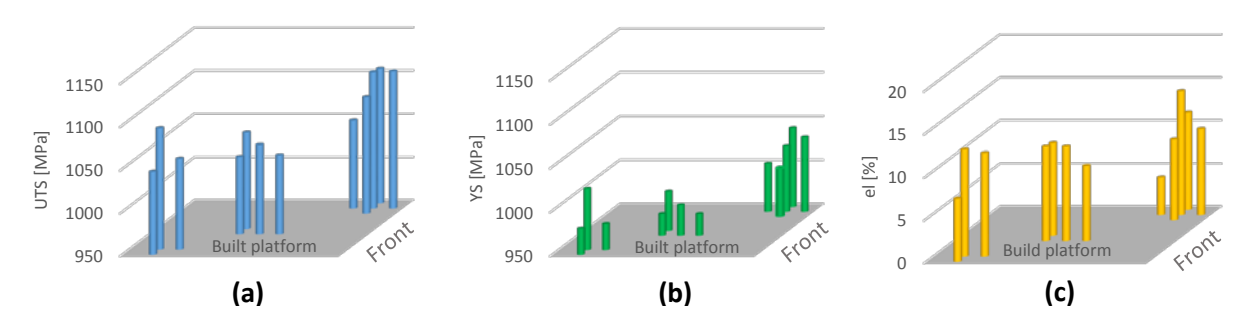


Figure 13. Tensile test results for vertically oriented specimens in different locations of the build platform: (a) UTS, (b) YS, (c) el %

Table 3. Tensile results and relative standard deviations for vertically oriented specimens at different locations on the build platform

	REAR CORNER		CEN	TER	FRONT CORNER		
	Average	RSD [%]	Average RSD [%]		Average	RSD [%]	
UTS [MPa]	1065	2.2	1050	1.0	1102	1.0	
YS [MPa]	993	2.3	983	1.0	1026	1.5	
el [%]	10.7	26.7	10.4	10.3	11.3	19.8	

3.4.3 Effect of orientation on strength and ductility

Tensile results from samples in different orientations were also compared in Table 4. Tensile strength values are similar for both orientations, however, noticeable differences were observed in the elongation values.

Table 4. Tensile test results with relative standard deviations for horizontal and vertical orientations. Typical properties for an annealed cast alloy [42] are also reported for comparison.

	HORIZONTAL		VERT	TCAL	CAST+ANNEALED
	Average	RSD [%]	Average	RSD [%]	CASTTANNILALLD
UTS [MPa]	1066	0.9	1073	2.6	930
YS [MPa]	1006	2.9	1001	2.5	855
el [%]	15.0	12.9	10.8	17.6	12

Fracture cross-sections of the specimens with the highest and lowest ductility were compared in order to identify the cause of the observed differences. Fracture surface of horizontally oriented sample shows significant necking and ductile dimples, Figure 14a. However, the vertically oriented specimen, Figure 14b shows no necking and the fracture surface is flat in the center of the specimen, parallel to the scanning layers.

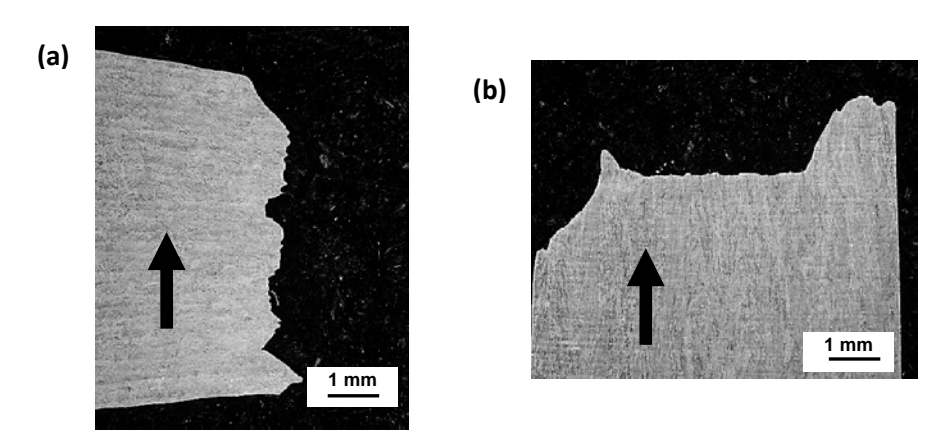


Figure 14. Fracture surfaces of (a) horizontal and (b) vertical oriented samples. Arrows indicate the build direction.

The surface of the vertically oriented specimen was further studied by SEM. Some discontinuous areas were detected on the fracture surface, Figure 15, where unmelted powder particles can be seen. The clustering of these non-sintered zones is the most probable cause for the lower ductility of the vertical specimens.

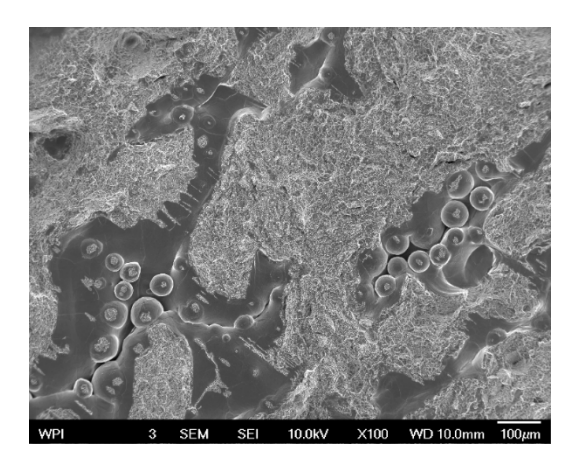


Figure 15. SEM image of the fracture surface of the vertical specimen, showing unmelted powder particles.

3.5 Effect of annealing time and temperature on the microstructure

The study of the microstructure at different distances from the build platform has revealed that α lath thickness increases at locations closer to the build platform. It is believed that the prolonged dwell time at the chamber temperature increases α lath thickness, creating a coarser microstructure.

To demonstrate this behavior an annealing experiment was performed. Annealing samples have been obtained from a location at 90 mm from the build platform. Samples with a $0.66\mu m$ α lath thickness have been annealed at 600° C, 700° C, and 800° C, and extracted at time periods between 10 and 120 hours. Vertical cross-sections of the samples were prepared for the microstructural study. The results, Figure 16, show the coarsening of α laths after exposing the lamellar $\alpha+\beta$ microstructure to temperatures above 600° C. This phenomenon explains why α lath thickness decreases with the distance from the build platform during the EBM process, at chamber temperature of 650° C. The locations closer to this platform remain longer time at the chamber temperature than the upper layers, so α laths are coarser.

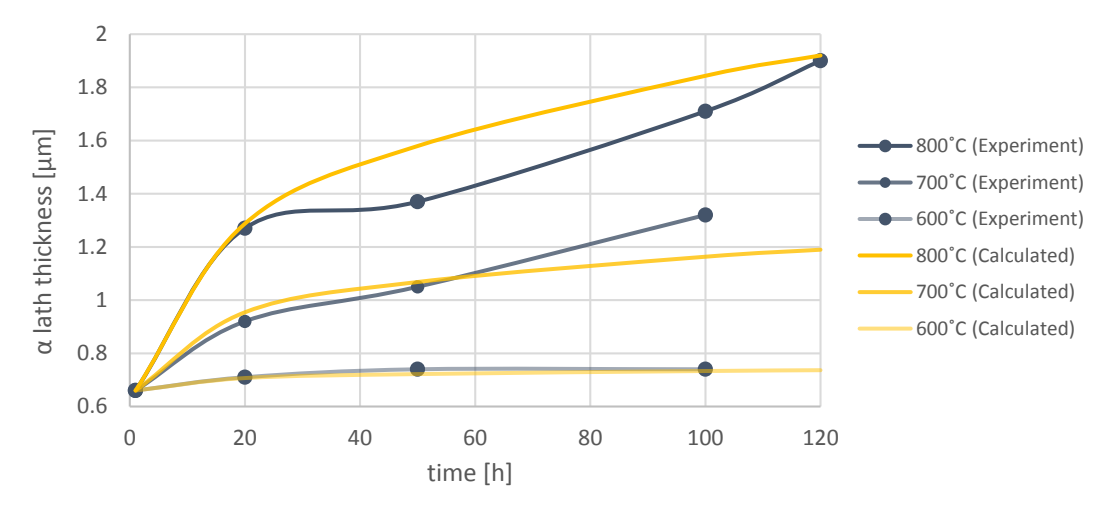


Figure 16. Experimental and calculated values of α lath thickness as a function of annealing time and temperature.

An empirical equation has been developed to relate α lath thickness with time and temperature.

$$\delta_{\alpha_{lath}} = \delta_{\alpha_{lath}(t=0)} \times t^{\left(\frac{T-850}{1000}\right)}$$

where $\delta_{\alpha lath}$ is α lath thickness (in microns) at the end of the annealing treatment, $\delta_{\alpha lath}$ (t=0) is α lath thickness of the starting material, t is the annealing time in hours and T is the annealing temperature in degrees Kelvin. Values calculated with this equation have been compared and validated with the measured values obtained during the experimental work, Figure 16.

4 DISCUSSION

The microstructural analysis on specimens at different locations relative to the build platform revealed that α lath thickness varies with the height or distance from the build platform. This variation was not observed at distances below 25 mm [16]. Murr et al. [41] reported a variation of the α lath thickness from 1.6 μ m to 3.2 μ m at 10 mm and 60 mm distance from the build platform. This phenomenon is attributed to the effect of the build platform on the thermal history of successive layers that are added to the part. It is suggested that the cooling rate increases significantly with distance from the build platform, and thinner α laths correspond to higher cooling rates [43].

However, in this work, the coarser α laths near the platform can be explained by the longer exposure of the lower layers to the build chamber temperature (typically 650-700°C) relative to the upper layers. This was confirmed with an annealing experiment where the relationship between time, temperature, and α lath thickness was studied. Considering that the $\beta \rightarrow \alpha + \beta$ transformation mechanism at low cooling rates is diffusional growth transformation [43], it can be reasoned that α lath coarsening can be thermally-activated. Therefore, coarsening occurs very slowly at temperatures below 600°C and is more pronounced at higher temperatures. However, the mechanism for this coarsening in isothermal annealing conditions is not totally understood.

It should be noted that the cooling history is more complex than a mere continuous cooling process. At the first stage of the cooling, a fast solidification happens in the range of 10^{3} °C·s⁻¹ to 10^{5} °C·s⁻¹[44], from the melt pool temperature to temperatures close to the build chamber temperature. During this stage, the new layer reheats or partially re-melts the material locally, depending on scanning parameters such as beam power, scanning velocity, spot size, etc. [45], [46]. The second heating stage is quasi-isothermal, where the temperature at a point varies only due to heat transfer from upper layers with subsequent passes of the electron beam. During this stage, α lath coarsening can occur. Finally, when the fabrication process is over, there is a slow cooling stage from the build chamber temperature to room temperature.

The first cooling stage is the most critical for the formation of the microstructure because both the β grain formation and $\beta \rightarrow \alpha + \beta$ transformations happen at temperatures above 850°C [9]. Although cooling rates are high enough to form the α' martensitic phase (4°C.s⁻¹) [9], the high temperature at the end of this stage (650-700°C) and the complex re-melting and re-heating periods inhibit the transformation of α into α' martensitic structure [18]. However, Al-Bermani et al. [44] observed localized α' martensitic microstructure on the top of small size EBM samples. The observation of some α' martensitic phase in the sample on the top surface is plausible because of the absence of upper layers that cause the reheating of the material, combined with the small size of the sample that enables greater cooling rates and the relatively short exposure of the α' phase to the chamber temperature.

No appreciable differences were observed between the microstructures of specimens located at the center and edge (interior and exterior) of the build platform, suggesting that the electron beam deflection does not have a significant effect on the temperature history of the samples. Hrabe et al. [15] had hypothesized a cooler build space could lead to greater cooling rates at the exterior part of the build platform relative to the interior, due to the increased electron beam deflection. They suggested slightly finer α laths for the exterior part of the build platform, which however has not been observed in this study.

In this work it has found that α lath thickness varies with distance from the build platform, however tensile properties and micro-hardness values were not affected. Additionally, microstructures did not change significantly with position in the XY plane, but significant variations were observed in tensile properties. These apparently contradictory results can be explained by considering that the main microstructural feature in the study, α lath thickness, is not the principal factor controlling the tensile properties.

Porosity has a considerable influence on mechanical properties of additive manufacturing parts, especially when subjected to cyclic loads, where porosity can act as crack nucleation site and lead to premature failure of the part [47]. Porosity occurs due to building defects and hollow powder particles. It was observed that build defects are most detrimental to mechanical properties when loading is applied along the build direction. This is because the unmelted areas are typically planar and normal to the build direction, acting as failure initiation sites and reducing mechanical properties. The observation of unmelted powder particles on the fracture surfaces of tensile specimens corroborates this statement.

Several methods have been employed for porosity or density measurements for AM parts. Spierings et al. [29] compared the Archimedes method, micrograph cross-section, and X-ray scanning. According to this study, there are significant differences in the results obtained from these three techniques. Slotwinski et al. [47] used an ultrasonic method to quantify the amount of porosity in additive manufactured parts and suggested that there is a lower limit in the size of porosity that can be detected by X-ray scanning. Leuders et al. [48] measured the porosity above 22 μm size of SLM (Selective Laser Melting) Ti-6Al-4V parts employing a computer tomography system. Kasperovich et al. [49] measured the SLM Ti-6Al-4V part porosity by employing micrograph study and computer tomography, for later comparison with the Archimedes method. They concluded that the Archimedes method does not provide sufficient accuracy and precision. Gong et al. [50] utilized Archimedes method to compare the relationship between process parameters and porosity in EBM and SLM Ti-6Al-4V parts. It is expected that the Archimedes method has higher reliability because it considers the whole volume, instead of 2D sections of the parts, however Archimedes method does not consider any morphology or distribution of the porosity that can help to identify the porosity source (powder, process, etc.). Despite being a destructive characterization method, 2D porosity measurement employing cut sections and image analysis software has been often performed before [29,49]. Variation of the measured porosity depending on the surface condition (polished vs. polished and etched), micrograph magnification, and selection of the cross-section has been reported. The methodology has been considered as valid in terms of qualitative (size and shape) and comparative measurements.

5 CONCLUSIONS

The research results presented in this study lead to the following conclusions:

- Tensile mechanical properties (UTS, YS, and elongation) are greater in the locations where porosity is lower.
- With 0.15% average porosity in the material, the differences between mechanical properties of the parts fabricated from different locations and distances from the build platform are mainly related to the porosity, the variations in the microstructure being of secondary importance.
- The variation in the microstructure has been related to the dwell time of the layers on the fabrication chamber, although this does not significantly affect the mechanical properties.
- In order to optimize EBM fabrication processes for component mechanical performance, fabrication process parameter algorithms should be designed to minimize porosity and unmelted areas.
- Further improvement of the EBM technology should be able to reconcile the differences in porosity between the center and edges of the build platform.

ACKNOWLEDGMENTS

This research was performed under the Additive Manufacturing program of the Integrative Material Design Center (iMdc) consortium at Worcester Polytechnic Institute, in collaboration with the Additive Manufacturing Demonstration Facility of Oak Ridge National Laboratory, and sponsored by the US Department of Energy, Office of Energy Efficiency and Renewable Energy, Advanced Manufacturing Office, under contract DE-AC05-00OR22725 with UT-Battelle, LLC. WPI students, Matthew Gleason (Surface Metrology Laboratory), Yuwei Zhai, and Anthony Spangenberger (iMdc) also collaborated actively in the characterization process performed during the research.

REFERENCES

- [1] Y. Zhai, D.A. Lados, J.L. LaGoy, Additive manufacturing: making imagination the major limitation, JOM. 66 (2014) 808–816.
- [2] ASTM-International, ASTM Standard F2792-12a: Standard Terminology for Additive Manufacturing Technologies, (2012).
- [3] J. Scott, N. Gupta, C. Weber, S. Newsome, T. Wohlers, T. Caffrey, Additive manufacturing: Status and opportunities, Science and Technology Policy Institute. (2012) 1–29.
- [4] D.L. Bourell, M.C. Leu, D.W. Rosen, Roadmap for additive manufacturing: identifying the future of freeform processing, The University of Texas, Austin. (2009).
- [5] National Institute of Standards and Technology (NIST), Measurement Science for Metal-Based Additive Manufacturing, 2013.

- [6] National Intelligence Council, Global Trends 2030: Alternative Worlds, 5 (2012).
- [7] AM Platform, Additive Manufacturing: Strategic Research Agenda, 2014.
- [8] T.R. Mahale, Electron beam melting of advanced materials and structures [dissertation], North Carolina State University, 2009.
- [9] J. Sieniawski, W. Ziaja, K. Kubiak, M. Motyka, Microstructure and mechanical properties of high strength two-phase titanium alloys, Titanium Alloys-Advances in Properties Control. (2013) 69–80.
- [10] L. Facchini, E. Magalini, P. Robotti, A. Molinari, Microstructure and mechanical properties of Ti-6Al-4V produced by electron beam melting of pre-alloyed powders, Rapid Prototyping Journal. 15 (2009) 171–178.
- [11] M. Koike, K. Martinez, L. Guo, G. Chahine, R. Kovacevic, T. Okabe, Evaluation of titanium alloy fabricated using electron beam melting system for dental applications, Journal of Materials Processing Technology. 211 (2011) 1400–1408.
- [12] X. Gong, T. Anderson, K. Chou, Review on Powder-Based Electron Beam Additive Manufacturing Technology, in: ASME/ISCIE 2012 International Symposium on Flexible Automation, 2012: pp. 507–515.
- [13] B.S. Bass, Validating the Arcam EBM process as an alternative fabrication method for titanium-6Al-4V alloys [dissertation], North Carolina State University, 2008.
- [14] P. Edwards, A. O'Conner, M. Ramulu, Electron beam additive manufacturing of titanium components: Properties and performance, Journal of Manufacturing Science and Engineering. 135 (2013) 061016.
- [15] N. Hrabe, T. Quinn, Effects of processing on microstructure and mechanical properties of a titanium alloy (Ti-6Al-4V) fabricated using electron beam melting (EBM), Part 2: Energy input, orientation, and location, Materials Science and Engineering: A. 573 (2013) 271–277.
- [16] N. Hrabe, T. Quinn, Effects of processing on microstructure and mechanical properties of a titanium alloy (Ti-6Al-4V) fabricated using electron beam melting (EBM), Part 1: Distance from build plate and part size, Materials Science and Engineering: A. 573 (2013) 264–270.
- [17] L. Murr, E. Esquivel, S. Quinones, S. Gaytan, M. Lopez, E. Martinez, et al., Microstructures and mechanical properties of electron beam-rapid manufactured Ti-6Al-4V biomedical prototypes compared to wrought Ti-6Al-4V, Materials Characterization. 60 (2009) 96–105.
- [18] H. Rafi, N. Karthik, H. Gong, T.L. Starr, B.E. Stucker, Microstructures and Mechanical Properties of Ti6Al4V Parts Fabricated by Selective Laser Melting and Electron Beam Melting, Journal of Materials Engineering and Performance. 22 (2013) 3872–3883.
- [19] S. Rengers, EBM vs DMLS, A closer examination of these Ti64 capable additive manufacturing technologies, 2012.

- [20] M. Svensson, U. Ackelid, A. Arcam, Titanium alloys manufactured with electron beam melting mechanical and chemical properties, in: Materials and Processes for Medical Devices Conference(MDM V), ASM International, Minneapolis, MN, 2010: pp. 189–194.
- [21] S. Rawal, J. Brantley, N. Karabudak, Additive manufacturing of Ti-6Al-4V alloy components for spacecraft applications, in: Recent Advances in Space Technologies (RAST), 2013 6th International Conference on, 2013: pp. 5–11.
- [22] S. Hashmi, Comprehensive Materials Processing, Newnes, 2014.
- [23] P. Nandwana, W.H. Peter, R.R. Dehoff, L.E. Lowe, M.M. Kirka, F. Medina, et al., Recyclability study on Inconel 718 and Ti-6Al-4V powders for use in electron beam melting, Metallurgical and Materials Transactions B. (2015) 1–9.
- [24] ASTM-International, ASTM Standard F136-13: Standard Specification for Wrought Titanium-6Aluminum-4Vanadium ELI (Extra Low Interstitial) Alloy for Surgical Implant Applications, (2003).
- [25] Ti6Al4V ELI Titanium Alloy data sheet, (n.d.). www.arcam.com.
- [26] ISO-ASTM, ISO/ASTM 52921:2013: Standard Terminology for Additive Manufacturing-Coordinate Systems and Test Methodologies, (2013).
- [27] N.S. Claxton, T.J. Fellers, M.W. Davidson, Laser scanning confocal microscopy, Department of Optical Microscopy and Digital Imaging, Florida State University, Tallahassee. (2006).
- [28] G. Vander Voort, A. Roosz, Measurement of the interlamellar spacing of pearlite, Metallography. 17 (1984) 1–17.
- [29] A. Spierings, M. Schneider, R. Eggenberger, Comparison of density measurement techniques for additive manufactured metallic parts, Rapid Prototyping Journal. 17 (2011) 380–386.
- [30] ASTM-International, ASTM Standard E8/E8M-09: Standard Test Methods for Tension Testing of Metallic Materials, (2009).
- [31] A. Safdar, Microstructures and surface roughness of EBM produced Ti-6Al-4V, Solid Mechanics, Lund University, 2010.
- [32] J. Karlsson, A. Snis, H. Engqvist, J. Lausmaa, Characterization and comparison of materials produced by Electron Beam Melting (EBM) of two different Ti-6Al-4V powder fractions, Journal of Materials Processing Technology. 213 (2013) 2109–2118.
- [33] K.S. Chan, M. Koike, R.L. Mason, T. Okabe, Fatigue Life of Titanium Alloys Fabricated by Additive Layer Manufacturing Techniques for Dental Implants, Metallurgical and Materials Transactions A. 44 (2013) 1010–1022.
- [34] P. Edwards, M. Ramulu, Fatigue Performance Evaluation of Selective Laser Melted Ti-6Al-4V, Materials Science and Engineering: A. (2014).

- [35] J. Springer, In vitro Studies of Titanium Alloy Discs Fabricated with Electron Beam Melting for Improving Transdermal Osseointegrated Implant Surfaces [dissertation], North Carolina State University, (2010).
- [36] U. Ackelid, M. Svensson, Additive manufacturing of dense metal parts by electron beam melting, in: Materials Science and Technology (MS&T) Conference, 2009.
- [37] M. Rooney, R.M. Deacon, E.D. LaBarre, A.M. Lennon, M.P. Boyle, An evaluation of select material properties for electron beam melted Ti-6Al-4V, 2009.
- [38] H. Weiwei, J. Wenpeng, L. Haiyan, T. Huiping, K. Xinting, H. Yu, Research on Preheating of Titanium Alloy Powder in Electron Beam Melting Technology, Rare Metal Materials and Engineering. 40 (2011) 2072–2075.
- [39] A. Bauereiß, T. Scharowsky, C. Körner, Defect generation and propagation mechanism during additive manufacturing by selective beam melting, Journal of Materials Processing Technology. 214 (2014) 2522–2528.
- [40] H. Gong, K. Rafi, T. Starr, B. Stucker, The Effects of Processing Parameters on Defect Regularity in Ti-6Al-4V Parts Fabricated By Selective Laser Melting and Electron Beam Melting, (2013).
- [41] L. Murr, E. Esquivel, S. Quinones, S. Gaytan, M. Lopez, E. Martinez, et al., Microstructures and mechanical properties of electron beam-rapid manufactured Ti-6Al-4V biomedical prototypes compared to wrought Ti-6Al-4V, Materials Characterization. 60 (2009) 96–105.
- [42] P.A. Kobryn, Casting of Titanium Alloys, 1996.
- [43] G. Lütjering, J.C. Williams, Titanium, Springer, 2003.
- [44] S. Al-Bermani, M. Blackmore, W. Zhang, I. Todd, The origin of microstructural diversity, texture, and mechanical properties in electron beam melted Ti-6Al-4V, Metallurgical and Materials Transactions A. 41 (2010) 3422–3434.
- [45] M. Zäh, S. Lutzmann, M. Kahnert, F. Walchshäusl, Determination of Process Parameters for Electron Beam Sintering (EBS), in: Excerpt from the Proceedings of the COMSOL Conference Hannover, 2008.
- [46] A. Safdar, A study on Electron Beam Melted Ti-6Al-4V, 2012.
- [47] J.A. Slotwinski, E.J. Garboczi, K.M. Hebenstreit, Porosity Measurements and Analysis for Metal Additive Manufacturing Process Control, (n.d.).
- [48] S. Leuders, M. Thöne, A. Riemer, T. Niendorf, T. Tröster, H. Richard, et al., On the mechanical behaviour of titanium alloy TiAl6V4 manufactured by selective laser melting: Fatigue resistance and crack growth performance, Int. J. Fatigue. 48 (2013) 300–307.

- [49] J.H. G. Kasperovich, Improvement of fatigue resistance and ductility of TiAl6V4 processed by selective laser melting, Journal of Materials Processing Technology. (2015).
- [50] H. Gong, K. Rafi, H. Gu, T. Starr, B. Stucker, Analysis of defect generation in Ti-6Al-4V parts made using powder bed fusion additive manufacturing processes, Additive Manufacturing. 1 (2014) 87–98.